Journal of The Electrochemical Society

The Electrochemical Society
Advancing solid state & electrochemical science & technology

OPEN ACCESS

Thermal Runaway of Li-Ion Cells: How Internal Dynamics, Mass Ejection, and Heat Vary with Cell Geometry and Abuse Type

To cite this article: Matthew Sharp *et al* 2022 *J. Electrochem. Soc.* **169** 020526

View the article online for updates and enhancements.

You may also like

- Operando Analysis of Thermal Runaway in Lithium Ion Battery during Nail-Penetration Test Using an X-ray Inspection System
Tokihiko Yokoshima, Daikichi Mukoyama, Fujio Maeda et al.
- Modeling Nail Penetration Process in Large-Format Li-Ion Cells
Wei Zhao, Gang Luo and Chao-Yang Wang
- Understanding Li-Ion Cell Internal Short Circuit and Thermal Runaway through Small, Slow and In Situ Sensing Nail Penetration
Shan Huang, Xiaoniu Du, Mark Richter et al.

We Advance Battery Research!

EL-CELL®
electrochemical test equipment

- Electrochemical Battery Test Cells
- Multi-channel Potentiostats / Galvanostats / EIS
- Tools, Consumables & Testing Services

el-cell.com +49 40 79012-734 sales@el-cell.com

This content was downloaded from IP address 144.82.114.226 on 30/10/2023 at 12:54

Journal of The Electrochemical Society, 2022 **169** 020526

Thermal Runaway of Li-Ion Cells: How Internal Dynamics, Mass Ejection, and Heat Vary with Cell Geometry and Abuse Type

Matthew Sharp,[1] John Jacob Darst,[2] Peter Hughes,[2] Julia Billman,[1] Martin Pham,[3] David Petrushenko,[2] Thomas M. M. Heenan,[3,4] Rhodri Jervis,[3,4] Rhodri Owen,[3,4] Drasti Patel,[3] Du Wenjia,[3,4] Harry Michael,[3,4] Alexander Rack,[5] Oxana V. Magdysyuk,[6] Thomas Connolley,[6] Dan J. L. Brett,[3,4] Gareth Hinds,[7] Matt Keyser,[1] Eric Darcy,[2] Paul R. Shearing,[3,4] William Walker,[2] and Donal P. Finegan[1,z]

[1]*National Renewable Energy Laboratory, 15013 Denver W. Parkway, Golden, CO 80401, United States of America*
[2]*National Aeronautical Space Administration, Johnson Space Center, 2101 E NASA Pkwy, Houston, TX 77058, United States of America*
[3]*Electrochemical Innovation Laboratory, University College London, Torrington Place, London WC1E6BT, United Kingdom*
[4]*The Faraday Institution, Harwell Science and Innovation Campus, Didcot, OX11 0RA, United Kingdom*
[5]*ESRF—The European Synchrotron, 38000 Grenoble, France*
[6]*Diamond Light Source, Harwell Science and Innovation Campus, Didcot OX11 0DE, United Kingdom*
[7]*National Physical Laboratory, Teddington, TW11 0LW, United Kingdom*

Thermal runaway of lithium-ion batteries can involve various types of failure mechanisms each with their own unique characteristics. Using fractional thermal runaway calorimetry and high-speed radiography, the response of three different geometries of cylindrical cell (18650, 21700, and D-cell) to different abuse mechanisms (thermal, internal short circuiting, and nail penetration) are quantified and statistically examined. Correlations between the geometry of cells and their thermal behavior are identified, such as increasing heat output per amp-hour (kJ Ah^{-1}) of cells with increasing cell diameter during nail penetration. High-speed radiography reveals that the rate of thermal runaway propagation within cells is generally highest for nail penetration where there is a relative increase in rate of propagation with increasing diameter, compared to thermal or internal short-circuiting abuse. For a given cell model tested under the same conditions, a distribution of heat output is observed with a trend of increasing heat output with increased mass ejection. Finally, internal temperature measurements using thermocouples embedded in the penetrating nail are shown to be unreliable thus demonstrating the need for care when using thermocouples where the temperature is rapidly changing. All data used in this manuscript are open access through the NREL and NASA Battery Failure Databank.
© 2022 The Author(s). Published on behalf of The Electrochemical Society by IOP Publishing Limited. This is an open access article distributed under the terms of the Creative Commons Attribution 4.0 License (CC BY, http://creativecommons.org/licenses/by/4.0/), which permits unrestricted reuse of the work in any medium, provided the original work is properly cited. [DOI: 10.1149/1945-7111/ac4fef]

Manuscript submitted November 10, 2021; revised manuscript received January 3, 2022. Published February 9, 2022.

Supplementary material for this article is available online

Lithium-ion (Li-ion) batteries are used for a wide range of applications where their safety and reliability are of utmost importance, such as for human space flight,[1] electric vehicles,[2] and portable electronics. Designing safe battery systems that can prevent catastrophic failure events like thermal runaway is critical for the success of such applications, where failure can compound to life-threatening scenarios or have severe socio-economic consequences.[3,4] Electric vehicle researchers from Volkswagen and Ford emphasized the importance of more detailed and cost-effective testing and modelling methods for understanding the risks posed by thermal runaway to design safer battery systems.[2,5] To address this challenge, manufacturers of battery systems need to have a comprehensive understanding of the range of possible thermal runaway behavior of their selected cells. Furthermore, they need to be aware of the risks posed by such behavior to design a safe battery system that can contain the initial event and prevent propagation of thermal runaway while achieving favorable energy and power densities.

Different types of Li-ion cells (manufacturer, geometry, and model) behave differently during thermal runaway[6] and recent work has shown that a single type of cell repeatedly tested under similar abuse conditions can display a distribution of heat output and temperatures,[7,8] demonstrating the need for conducting statistically significant quantities of repeat tests and performing statistical analyses of battery failure parameters. Understanding the distribution of parameters like heat output during thermal runaway is further complicated by there being numerous abuse testing methods. These testing methods, including thermal abuse, internal short circuiting, and mechanical abuse, and add another layer of complexity when trying to characterize thermal runaway in each cell. This, as well as the numerous cell geometries and designs of battery enclosures, ultimately increases the variability in thermal runaway reactions and complicates interpretation of results. Consequently, consistency of testing conditions and the representativeness of test results for simulating field-failures such as internal short circuits remains a topic of debate for defining test standards.[9] Furthermore, since traditional calorimetry methods such as accelerated rate calorimetry (ARC)[10,11] take single measurements of heat during a failure event, little is understood about how the heat is distributed between ejected and non-ejected material. A detailed description of where the heat and ejected materials are displaced is critical for understanding the risks posed by a single-cell failure event inside a module. A fractional breakdown of ejected and non-ejected heat is also needed to validate detailed multi-physics models of thermal runaway.[12,13] Additionally, high sample numbers are needed for statistical significance. While some previous studies[14,15] documented trends in thermal runaway behaviors with high sample numbers, none have established the fraction of heat ejected, mass ejected, and the internal dynamics of cells during failure.

A Fractional Thermal Runaway Calorimeter (FTRC) was previously developed[8] to quantitatively evaluate thermal runaway energy release in the form of total energy yield vs fractions of that released through the ejected contents and that of the non-ejected contents; data acquired provides greater insight into how heat distributes throughout a battery system during thermal runaway. This enabled a distinction between estimates of the amount of heat that would dissipate from the cell through interstitial heat sinks, and heat that would be ejected by other means. This capability

[z]E-mail: donal.finegan@nrel.gov

distinguishes the capabilities from FTRC from more traditional calorimetric methods that provide a single value for total heat output. The FTRC was also designed to be compatible with high-speed X-ray imaging[7,16–19] to link dynamic phenomena that occur within cells during thermal runaway to measurements taken externally, such as heat distribution and temperatures. In addition to thermal abuse, the FTRC was also designed to be compatible with nail penetration tests, which when combined with customized nails with embedded thermocouples[17,20] also facilitated temperature measurements from inside the cell during thermal runaway. Ejected mass is also captured within the FTRC and measured following each test, giving data on post-test ejected mass and remaining cell mass. Thus, the FTRC coupled with high-speed radiography provides an effective means to characterize the tendency of cells to eject heat and mass, as well as an opportunity to view how the process of thermal runaway evolves in real time within the cell. The National Renewable Energy Laboratory (NREL) and National Aeronautics and Space Administration (NASA) have made data from hundreds of FTRC tests open access,[21] some of which is described in this work.

In this work, we draw from the Battery Failure Databank[21] to explore the differences between failure mechanisms of different cell types tested under different abuse conditions, with respect to thermal behavior, mass ejected, and internal structural dynamics. We examine the behavior of 3 different geometries of cells (18650, 21700, and D-cell) exposed to 3 different abuse types (thermal abuse, internal short circuiting,[16] and nail penetration) to quantitatively describe their respective responses to the different trigger methods. For each cell, we extracted data from the Battery Failure Databank, including the fractions of ejected and non-ejected heat, the fractions of ejected and non-ejected masses, internal temperatures during nail penetration, and directional velocities of thermal runaway propagation within the cells as estimated from high-speed synchrotron X-ray radiography. Correlations between mass ejected and heat output are assessed, as well as how the abuse mechanism influences the heat generation and mass ejection of cells. Finally, trends associated with the three different geometries of cells are quantified, with respect to normalized heat output (kJ Ah^{-1}), fraction of mass ejected, and the rate at which thermal runaway propagates within the cell casing. It is expected that these data will help elucidate the variability in cell responses to different abuse conditions and clarify the differences in behavior observed for various cell geometries.

Methods

All data used in this work were sourced from the Battery Failure Databank.[21] This databank contains heat output, mass ejection, and temperature data that was collected from FTRC experiments conducted at synchrotron facilities. Most tests also have an associated X-ray radiography video that provides insight into the dynamic phenomena that occur within cells during thermal runaway. The combination of FTRC data and radiography facilitates creating a link between the thermal and ejection response of the cell, and the events occurring within the cell body during thermal runaway.

Cell types and specifications.—The Li-ion cells chosen for this study were the KULR 18650-K330, the KULR 21700-K500, the LG 21700-M50, and the Saft D-Cell-VES16. All cells were tested within one year of manufacture and were supplied directly from the manufacturers. These cylindrical cells represent a range of geometries for examining how thermal runway varies within cells of different designs and dimensions. It should be mentioned that all these cells are high energy-density cells. With that said, repeat tests were conducted for each cell type, and with the continued expansion of the Battery Failure Databank, further cells will be added for comparison in the future. At the time that this study was conducted, the aforementioned cells have the most data available and can provide the most complete picture for cells of different geometries. The properties of each cell examined as well as the total number of tests for each cell type under each trigger methods are provided in Table I.

Cell testing conditions.—The FTRC was designed to facilitate various abuse test conditions for comparing thermal runaway response to different trigger methods including nail penetration, internal short circuit (ISC) device combined with external heat,[14] and thermal abuse. The nail penetration trigger method was performed using an adapter that was attached to the side of the cell chamber of the FTRC. This adapter enabled the nail to be inserted and retracted from the cell body on demand. To perform thermal abuse tests on the cells, heating elements were incorporated into the walls of the cell chamber of the calorimeter, a design which is described in more detail in previous work.[8] The heaters provided around 960 W until the cells underwent thermal runaway at which point the heaters were switched off. The thermal runaway reaction was then able to continue unimpeded to completion. The ISC trigger method consisted of an ISC device described in previous work.[16] Test cells were specially manufactured to incorporate the ISC device six layers into the wound electrode assembly. To activate the ISC device, the heating elements were switched on until the wax layer separating the current collectors melted (at approximately 57 °C), creating an internal short circuit that consistently initiated thermal runaway.

Heat, temperature, and mass measurements.—The FTRC was used to decouple the heat ejected from the cells and the heat emitted from the casing of the cells. The design of the FTRC to facilitate these distinct measurements is described in previous work.[7,8] The

Table I. (top) Specifications of cells assessed where all cells were at 100% state of charge (SOC). (bottom) Number of repeat tests for each cell conducted for each trigger method.

Cell Type	KULR 18650-K330 (BV)	KULR 21700-K500 (BV)	LG 21700-M50 (BV)	Saft D-Cell-VES16
Cell Format	18650	21700	21700	D-Cell
Diameter (mm)	18	21	21	33
Height (mm)	65	70	70	60
Volume (cm^3)	16.54	24.25	24.25	51.32
Negative vent?	Yes	Yes	Yes	No
Capacity (Ah)	3.3	5.0	5.0	4.5
100% SOC Voltage (V)	4.2	4.2	4.2	4.2
Average initial mass (g)	47.05	72.14	68.38	111.89
Cathode material	NCA	NCA	NMC	NCA
Anode material	Graphite	Graphite	Graphite-SiO_x	Graphite
Thermal tests	10	6	8	9
ISC tests	9	10	0	9
Nail tests	3	11	5	9

FTRC is also constructed of aluminum, allowing simultaneous X-ray imaging during tests (Fig. 1a). This provided distinct measurements for heat ejected from the positive end, heat emitted from the cell casing, and heat ejected from the negative end. For nail penetration tests, a modified nail with an embedded thermocouple near its tip was used for simultaneous internal temperature measurement during the tests. The design of the temperature-measuring nail is described in more detail in previous work.[17,20] By slowing the flow of ejected contents via a system of baffles and copper mesh in the ejecta bore chamber of the FTRC (see previous work[17,20]), the FTRC also captured ejected collectible mass such as aerosol matter, particulate, carbonaceous material, and shreds of current collector (Fig. 1b). Composition analysis and fractional contributions of particulate, aerosols, and carbonaceous matter in the collected mass are beyond the scope of this work, but a detailed breakdown of ejected solids from Li-ion cells undergoing thermal runaway can be found in work by Barone et al.[22] and Premnath et al.[23] The collected mass may also include some absorbed volatiles but most volatiles and aerosol particulate of <100 nm diameter were likely lost through the fume extraction. Following the completion of thermal runaway, the FTRC was disassembled and the cell mass distribution throughout the calorimeter was assessed. The mass of the collected material was measured gravimetrically on a microbalance. A photograph of a recovered cell, as well as an example of mass collection from the bore chamber are shown in Figs. 1c–1d. Any mass caught in the baffles and copper mesh is recovered and measured. This is defined as positive or negative ejecta, with positive or negative being determined by which terminal the mass was ejected from. Any mass remaining in the cell casing is defined as cell body mass. By finding the difference between the pre-test mass and the sum of cell body mass, positive ejecta, and negative ejecta, the mass of gases released is determined and defined as unrecovered mass; note that FTRC calculations are designed to estimate the energy contained within these unrecovered components. This mass accounts for the gases and solids (such as aerosols) which left the system during the tests. Data from the specific tests can be extracted from the Battery Failure Databank where specific test identifiers are listed in Supplementary Information (available online at stacks.iop.org/JES/169/020526/mmedia).

X-ray radiography.—High-speed radiography took place at ESRF—The European Synchrotron and Diamond Light Source Synchrotron. At the ESRF, a polychromatic beam of 76 keV was used for high-speed radiography at beamline ID19, with a high-speed PCO.Dimax (PCO AG, Germany) detector and LuAG:Ce ($Lu_3Al_5O_{12}$) scintillator. The FOV was 22.89 mm $\times$ 14.67 mm (horizontal $\times$ vertical) which consisted of 2016 $\times$ 1292 pixels with an isotropic pixel size of 11.35 μm. Images were captured at a rate of 2000 frames per second (fps) (with an exposure time of 461 μs). At Diamond Light Source, a monochromatic beam of 75 keV at beamline I12, along with a Vision Research Phantom Miro 310 high-speed detector (Vision Research, NJ, USA) and LuAG:Ce scintillator, were used. The cells were imaged with a FOV of 22.91 mm $\times$ 14.32 mm consisting of 1280 $\times$ 800 pixels (horizontal $\times$ vertical) with an isotropic pixel size of 17.9 μm, at 2000 fps using an exposure time of 490 μs. Radiography videos were flat-field corrected and timestamped using MATLAB, and are open access in the Battery Failure Databank.[21]

Results

Three cell geometries were examined, the properties of which are provided in Table I. This selection of cells tested under 3 different trigger methods (thermal, ISC, and nail penetration) facilitated comparisons of the response of different cell geometries to different trigger methods of thermal runaway. The cells are compared with respect to the mass ejected, the heat emitted, the distribution of heat between ejected and non-ejected materials, and the internal structural dynamics that were visualized from high-speed radiography.

Mass ejection from cells and correlation with heat output.—The mass ejection distributions for each cell can be seen in Fig. 2. As seen in Fig. 2a, each cell exhibited different characteristics regarding the mass ejected between trials. Overall, the Saft D-Cell was the most consistent, generally ejecting about 40 g of mass. The other cells showed more variability, with the LG 21700 ejected mass values having the largest distribution, spanning from roughly 30 g to 54 g across trials. This variability could potentially be linked to the rate at which thermal runaway propagated through the cell. This

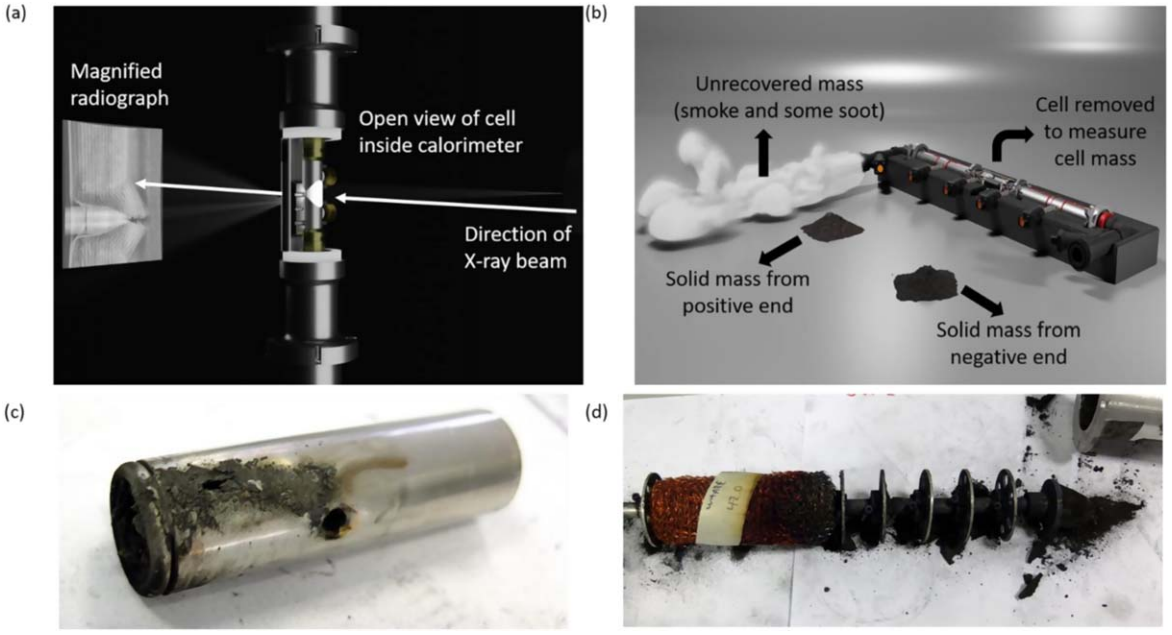

Figure 1. Experimental setup for the calorimeter used to obtain heat and mass measurements. (a) X-ray radiography provides internal views of thermal runaway. (b) View of the calorimeter assembled. Ejected solids were caught in baffles and copper mesh in the calorimeter (internal design of calorimeter discussed in previous work[8]). Solids were collected post-test and weighed, while gases were extracted and considered as unrecovered mass. (c) Photographs of an 18650 cell after thermal runaway and (d) its ejected mass being recovered from the baffles and mesh of the calorimeter, components of which were previously described.[7,8]

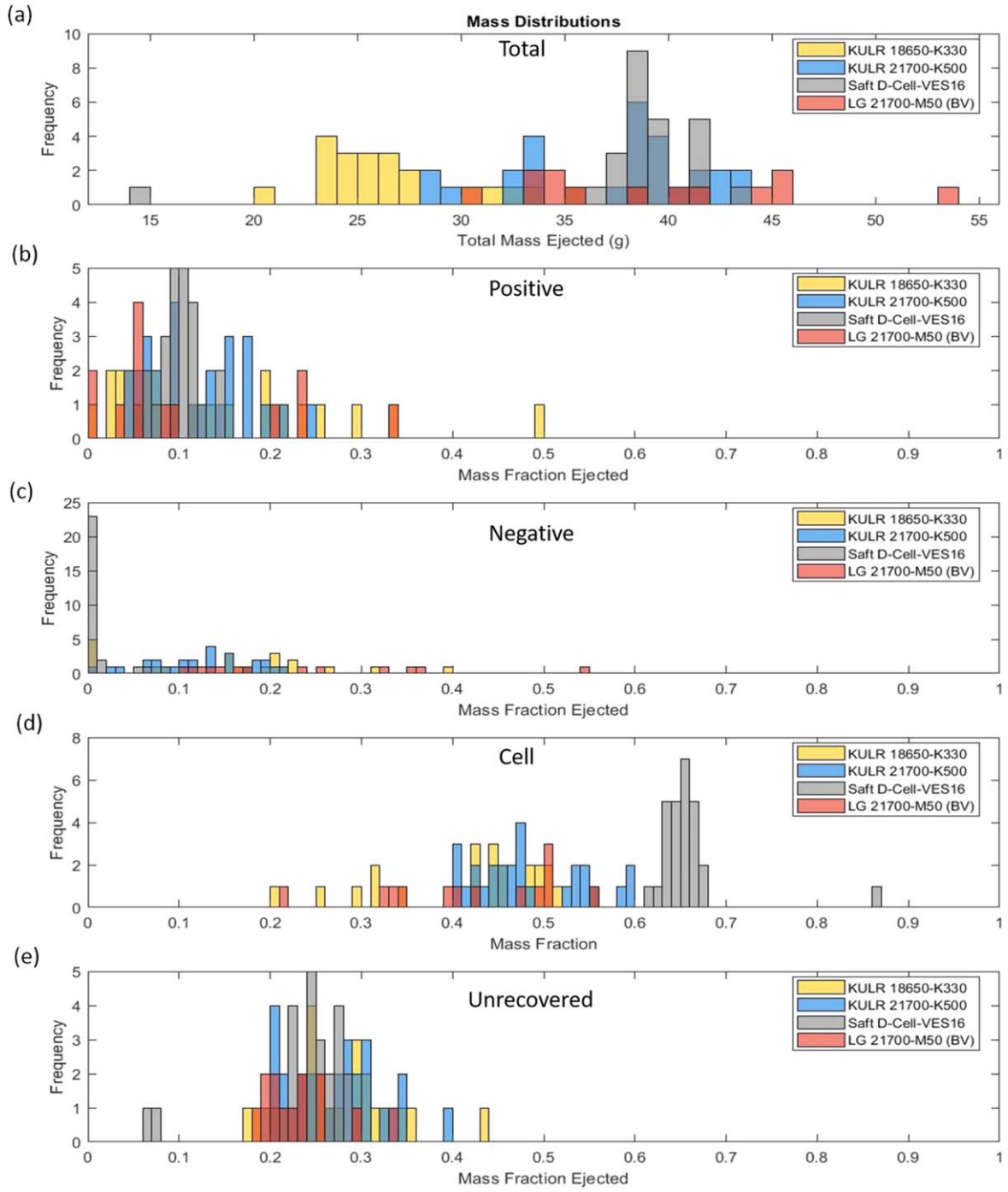

Figure 2. Histograms showing, for all trigger methods, (a) the total mass ejected from each cell in grams, (b) the mass fraction ejected from the positive end of each cell, (c) the mass fraction ejected from the negative end of each cell, (d) the mass fraction remaining within the cell casing following thermal runaway for each cell, and (e) the mass fraction of unrecovered mass for each cell. All data and accompanying radiography videos of the tests are available at the Battery Failure Databank.[24]

relationship will be discussed further when discussing the internal velocities as determined from radiography video.

To compare ejected mass values across cell type, the mass fraction ejected—that is the fraction of the cell's original mass that was ejected—is used in the remaining histograms. Figures 2b–2e display the mass fraction ejected from the positive end of the cell, the negative end, what remained within the cell casing, and the fraction of mass that went unrecovered (smoke, gas, and some particulate matter). While the data in Fig. 2 show the distribution of mass ejection behaviors, the donut plots in Fig. 3 provide better insight into the average behavior for each cell during thermal runaway.

The post-test mass distribution for each cell and trigger method is shown in Fig. 3a. The Saft D-Cell generally had the largest percentage of mass remaining within the cell body following the test, regardless of trigger method. This could potentially be due to the lack of a bottom vent on the D-Cell, albeit the D-cell had 2 top vents for pressure relief. All other cells in this study had a bottom vent which could play a vital role in ejecting mass from the cell body. Another consideration is the rate at which thermal runaway

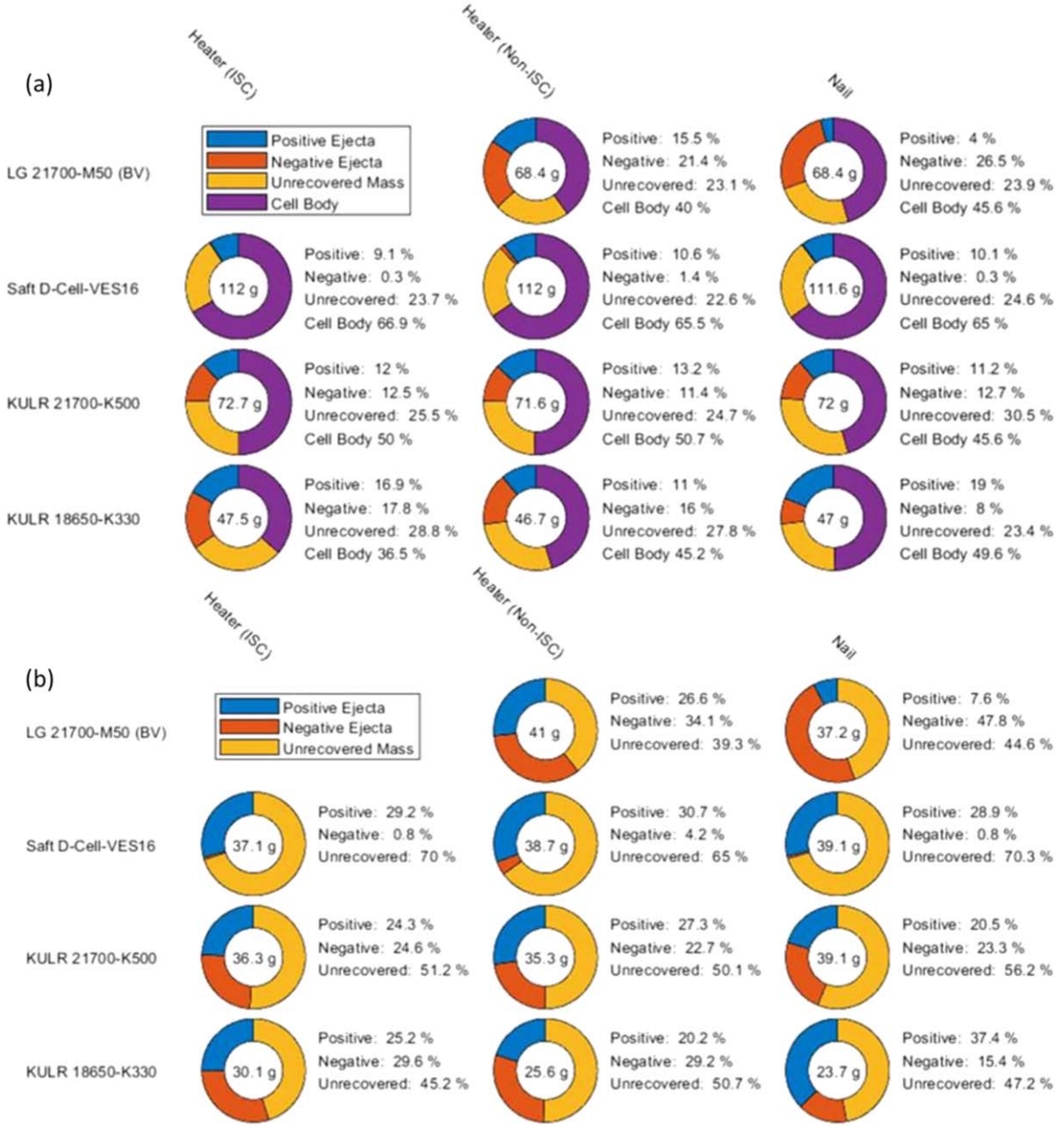

Figure 3. Donut plots representing the distribution of mass for each test cell and trigger method. Each column represents a different trigger method while each row represents a different cell type. (a) Distributions for all mass ejected from and remaining in the calorimeter following thermal runaway. (b) Distributions for all mass having been ejected from the cell casing.

progressed in the cell. The D-Cell had the slowest thermal runaway front velocities when compared to both the 18650 and 21700 cell formats, which will be discussed in more detail in a following section. This allowed for any gases that may have been produced during the reaction to escape the cell body at a rate that prevented the pressure within the casing from rising too high and causing a more violent cell rupture. This will be discussed further when addressing the velocities of thermal runaway propagation within each type of cell.

Referring to Fig. 3b, it is apparent the Saft D-Cell had the largest percentage of unrecovered mass of the four cells being considered. The Saft D-Cell was designed with more excess electrolyte than typical rechargeable 18650 cells to assist with achieving long cycle-life for space satellites. As the Saft D-Cell experiences high internal temperatures due to thermal runaway, the electrolyte evaporates by nature of its volatility, eventually venting from the cell and ejecting as unrecovered mass. The large quantity of unrecovered mass is unlikely to have been caused by relatively high internal temperatures during thermal runaway since radiography revealed that molten Cu was not observed to be widespread within the cell; Rather, the large quantity of unrecovered mass may be due to the cell having a higher ratio of electrolyte to active materials and hence a higher loss of volatile mass, the impact of which is discussed in greater detail by Ostanek et al.[12]

As for the KULR 18650, the nail penetration trigger method yielded a different ejected mass distribution than either the ISC or external heating mechanisms. Specifically, a greater mass is ejected from the positive end of the cell. Of the three nail penetration tests that were performed on this cell, only one of them resulted in activation of the bottom vent of the cell. This would suggest that internal pressures within the cell did not typically exceed the burst pressure of the vent. Instead, gases that accumulate and cause this pressure rise in thermal and ISC abuse tests would be able to escape through the hole in the cell casing created by the nail. The hole

produced by the nail may have acted as an additional vent, reducing the need for the bottom vent to activate.

The LG 21700 also displayed a disparity between the ejected mass distributions for the nail penetration and thermal trigger methods. The radiography footage shows that as the nail entered the cell, multiple instances of thermal runaway begin to propagate from various points of contact between the nail and the electrode assembly, a phenomenon that will be discussed in more detail in the following section on radiography. These multiple fronts of thermal runaway propagation would generate gas more quickly than a single front. Since the LG 21700 cell had an additional vent on the negative end of the casing, the pressure rose and activated both the positive and negative vents. Due to the larger area of the negative vent, it is expected that a higher rate of mass ejection occurred from the negative end of the cell.[18] For the thermal abuse test, the thermal runaway had a slower rate of propagation within the cell, producing gases at a lower rate. This resulted in activation of the negative vent at a later stage of the thermal runaway event, producing a more even distribution of mass between positive and negative ends of the cell.

Considering the mass ejection and the heat output from the cells in question, there are a few notable trends that appear. As seen in Fig. 4, the KULR 18650 displayed a wide range of mass ejections, with one group between 0.4 and 0.6 mass fraction ejected and another group situated from 0.6 to 0.8. The former group produced a lower heat output than the latter; that is, a higher heat output was observed for cells that ejected more mass. Referring to the associated radiography footage of the group producing larger heat output (radiographs can be found in the Battery Failure Databank[21] and specific test identifiers for the 18650 data plotted in Fig. 4 are provided in Supplementary Table SI), layers of the electrode assembly along the inner regions of the cell can be seen peeling away and flowing towards the positive or negative vent, whichever had opened. Eventually this process would essentially stop, suggesting flow through the vents had ceased, potentially due to clogging.[18] Clogging would have caused the pressure within the cell to build until rupturing, ejecting a higher mass fraction and heat output than cells whose vents remained clear throughout the entire reaction.

Another notable trend displayed in Fig. 4 is the variability of ejected mass fraction with respect to the cell diameter. Referring to the distributions along the *x*-axis, the D-Cell had the narrowest distribution of mass fraction being ejected while the 21700 formats had more variability. The 18650 ultimately displayed the highest degree of variability. This variability could be related to the area of the vents for each cell type, where a larger area would imply less resistance for the material to be ejected from the casing. Another consideration would be the rate at which pressure builds up within different cell volumes. For instance, if the rate of thermal runaway were constant for all cell types, pressure would still increase more rapidly in a smaller volume as compared to larger volumes. The rapid increase in pressure would increase the risk of a more uncontrolled rupture. This expected wider variation in internal pressure for smaller cells is expected to influence the mass ejected and heat output accordingly.

The Saft D-Cell produced the most heat when thermal runaway was initiated with the nail penetration trigger method. This is likely due to the nail inducing multiple fronts of thermal runaway that begin to propagate at the same time, i.e. a front that is observed to propagate from the surface of the nail along each electrode layer that it penetrated. This would result in greater heat output as the thermal runaway reaction is able to go further to completion before being ejected than thermal runaway events initiated with either thermal or ISC trigger methods. This trend can be seen in the other cells as well. In fact, the larger the cell diameter, the larger the difference in heat output between nail penetration and thermal trigger methods.

There appears to be a positive correlation between the ejected mass and heat output of the cells during thermal runaway for the 18650 and 21700 cells, with the D-cell being the exception to this correlation. As ejected mass increases, the heat output generally increases regardless of trigger method. This could potentially be due to a lack of oxygen within the cell. A lack of oxygen would stunt thermal runaway and prevent the reaction from running to completion, i.e. oxygen-limited reactions. If a cell containing such a stunted reaction were to rupture, its contents would then be exposed to atmospheric oxygen allowing the reaction to run closer to completion. This would result in a relationship as seen in Fig. 3, where higher ejected mass values correspond to higher heat output during thermal runaway.

Estimating internal velocities of thermal runaway propagation from radiography.—Radiography provides further insight into thermal runaway and the events occurring inside the cell. By comparing radiography with the thermal response of cells for each thermal runaway event, relationships can be brought to light. To assess the correlation between the propagation of thermal runaway throughout the cell and mass ejected, reaction front velocity was

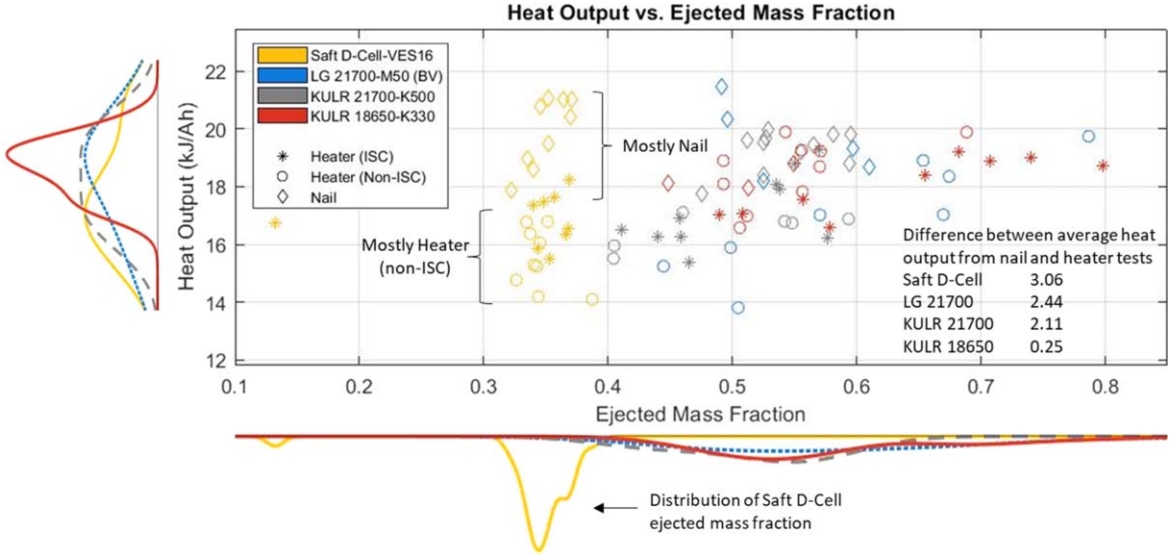

Figure 4. Comparison between heat output and ejected mass fraction. Cell types are distinguished by the color of the data points while trigger method is determined by the shape of the data points. Distributions along the axes provide further insight into the variability of ejected mass fraction and heat output for each cell type.

estimated using the radiography, as shown in Fig. 5. The front in this instance is taken to be the leading edge of the area within the cell that has thermally decomposed. Knowing the diameter of the cells, the distance of the reaction front from the outer radius of the cell was obtained with a corresponding timestamp. After some time had passed, the distance of the reaction front from the cell wall was again assessed, and a new timestamp was obtained. Using these values, the velocity of the front was roughly calculated. There is a large degree of uncertainty in these values, but they provide a qualitative comparison of rates of thermal runaway propagation within cells. It should be mentioned that not all tests had an accompanying radiography video that allowed for the calculation of velocities. The tests used to obtain velocity information are listed in Supplemental Information with their associated Battery Failure Databank[18] test identifiers.

After obtaining the speed of the fronts for as many tests as possible, the Saft D-Cell had the slowest thermal runaway propagation compared to any other cells while the LG 21700 had the fastest propagation. As previously discussed, the Saft D-Cell also has the largest percentage of post-test mass remaining within the cell casing while the LG 21700 has the smallest percentage. Taking both into consideration, the faster front propagation as seen in the LG 21700 produced gases at a more substantial rate than the cell was able to vent. As a consequence of internal pressure build-up, the cell would rupture carrying more of its mass out with it. Conversely, the slower thermal runaway propagation as seen in the Saft D-Cell created gases at a slower rate allowing the vents to properly expel the gases and prevent a more violent cell rupture.

Analysis of unrecovered mass across the different cells shows the Saft D-Cell created the largest percentage of unrecovered mass while the LG 21700 produced the least. Comparing this with the associated thermal runaway front velocities, it is apparent there exists an inverse relationship. While the LG 21700 may produce a large amount of gas within a small period of time, following ejection thermal runaway tapers off and gas production is reduced until it ceases altogether. In contrast, the Saft D-Cell produces gas for a longer period of time at a lower rate. This lower rate avoids rapid pressure build-up and bursting, preventing thermal runaway from prematurely ending and ultimately resulting in a larger unrecovered mass being generated.

While the general trend for thermal runaway velocity within the cell seems unrelated to cell geometry, there does seem to be a relationship with the cell energy density (Wh/kg). Plotting energy density against the average of the axial and radial velocities for each cell, a potential relationship can be seen (Fig. 6). As cell energy density increases, the average velocity of thermal runaway seems to increase, albeit with some exceptions. More information on electrode and electrolyte chemistry needs to become available before looking further into this possible relationship, which is challenging to determine in commercial cells.

Internal temperature estimations.—Having access to high-speed radiography provides a window into the internal happenings within the cell while thermal runaway is progressing. Looking at the radiography video for each cell being considered displays unique characteristics that would otherwise go unnoticed. For instance,

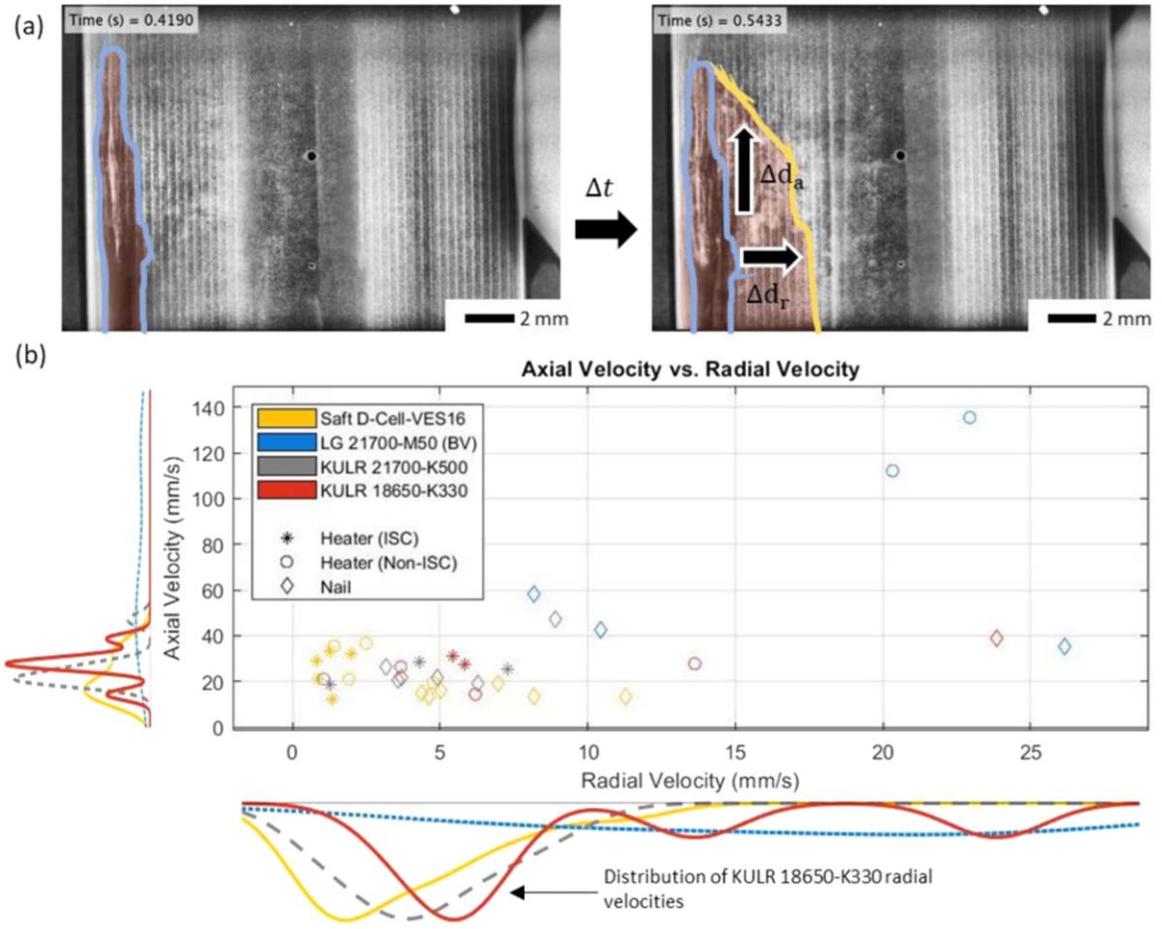

Figure 5. (a) Radiographs displaying the propagation of thermal runaway (red shading) in an 18650 cell. The left most edge of the shading is taken to be the reaction front. Arrows demonstrate the radial (horizontal) and axial (vertical) directions. (b) Comparison between radial and axial velocities within all cells. Radiography videos can be found for each test in the Battery Failure Databank[21] where test identifiers are provided in Supplementary Information for guidance.

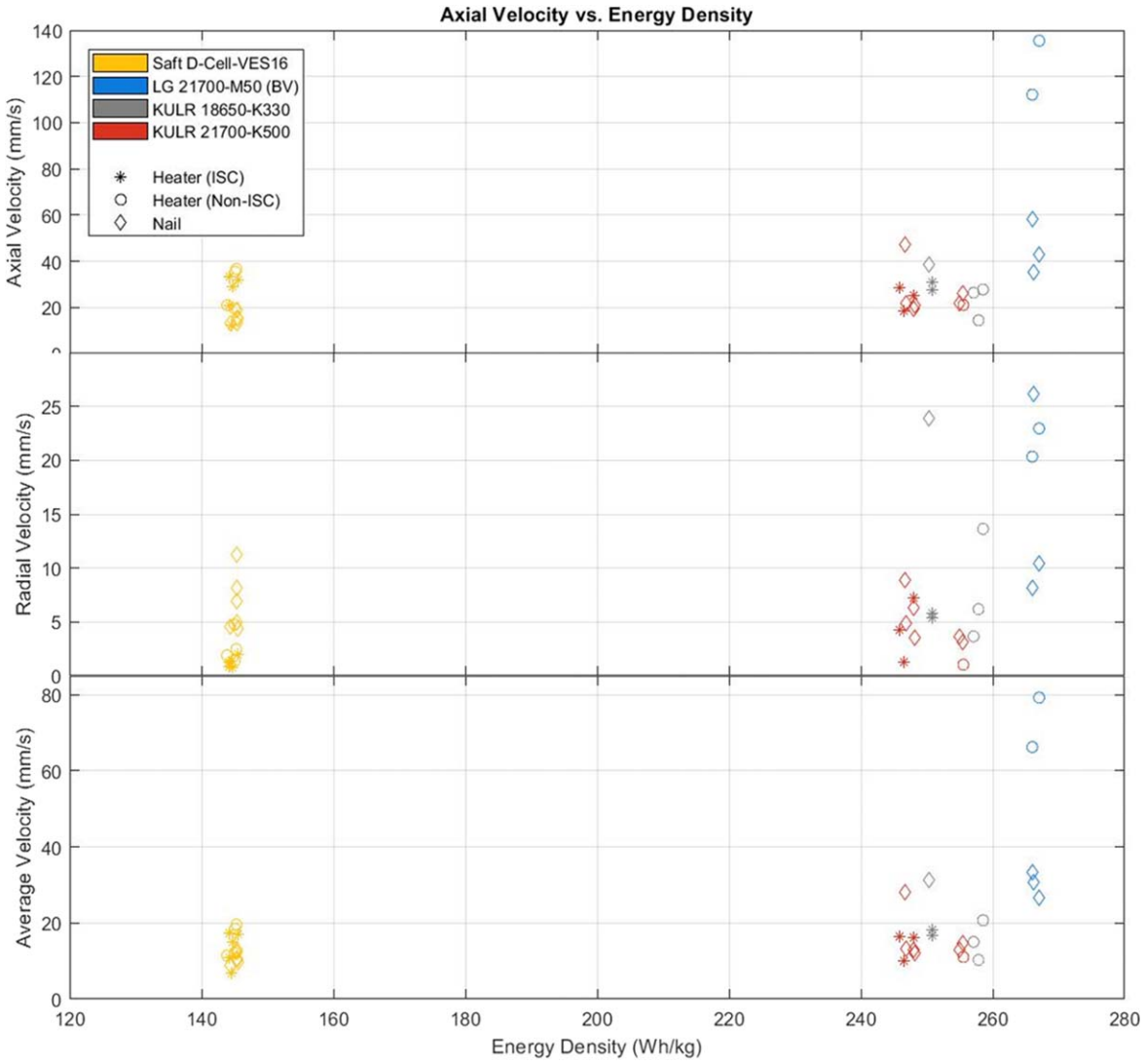

Figure 6. Comparison between thermal runway velocities in the axial (top), radial (middle), and average (bottom) directions and energy density within all battery cells.

whenever thermal runaway was initiated in the LG 21700 with the nail penetration trigger method, the layers of the jellyroll closest to the center of the cell always developed cracks and split before the nail was able to penetrate the layers itself. While this does not seem to have a noticeable impact on the mass ejected or remaining in the cell, this feature can have implications when attempting to model cells for simulations. Another notable feature that was seen in the radiography was the lack of molten copper globules in the Saft D-Cell tests (Fig. 7). Copper is evident in radiographs due to its relatively high attenuation of X-rays, while all other materials within Li-ion cells are much less attenuating. Molten copper, which is highly attenuating and shows up as white beads in radiography, was visible in only 5.5 percent of all the Saft D-Cell tests performed. This is opposed to molten copper being visible in 90 percent, 93.3 percent and 100 percent of the tests for the LG 21700, KULR 18650, and KULR 21700 cells, respectively. This is significant as it suggests the internal temperature of the cell as thermal runaway was progressing rarely exceeded 1080 °C (the melting point of copper) in the D-cells, regardless of trigger method. This disparity could potentially be due to the higher ratio of electrolyte to active material within the Saft D-Cell. This electrolyte would consume latent heat that would otherwise create higher internal temperatures in order to evaporate and exit the cell as unrecovered mass. The ability to obtain this result from the radiography becomes even more important when considering the lack of reliable internal temperature measurement techniques for these types of tests.

While the radiography videos provide evidence that all cells, with the exception of the Saft D-Cells, experienced internal temperatures greater than 1080 °C, thermocouples embedded in nails used for nail penetration tests show conflicting results. By inserting thermocouples into the center of hollowed out nails used in nail penetration tests, internal temperatures were recorded throughout the test. This practice is used to gather data on internal temperatures during thermal runaway which is useful for cell modelling. As seen in Figs. 8a–8b, these thermocouple readings were unreliable and rarely represented the actual internal cell temperatures. It should be mentioned that these data have been selectively chosen so that any discontinuous data (e.g. generated when a thermocouple broke or showed abnormal readings) is not presented. The IDs of the tests used in these plots can be found in Supplementary Information. Referencing the radiography video, molten copper can be seen flowing around the cell within 2 s of thermal runaway initiation for all but one of these tests (Fig. 8c). This suggests internal temperatures exceeded the 1080 °C melting point of copper, a temperature that was only recorded once by a thermocouple embedded within a nail (green in Figs. 8d–8e). The data from this single test is considered to be the most representative of internal temperatures during thermal runaway. The red plot in Figs. 8d–8e shows an

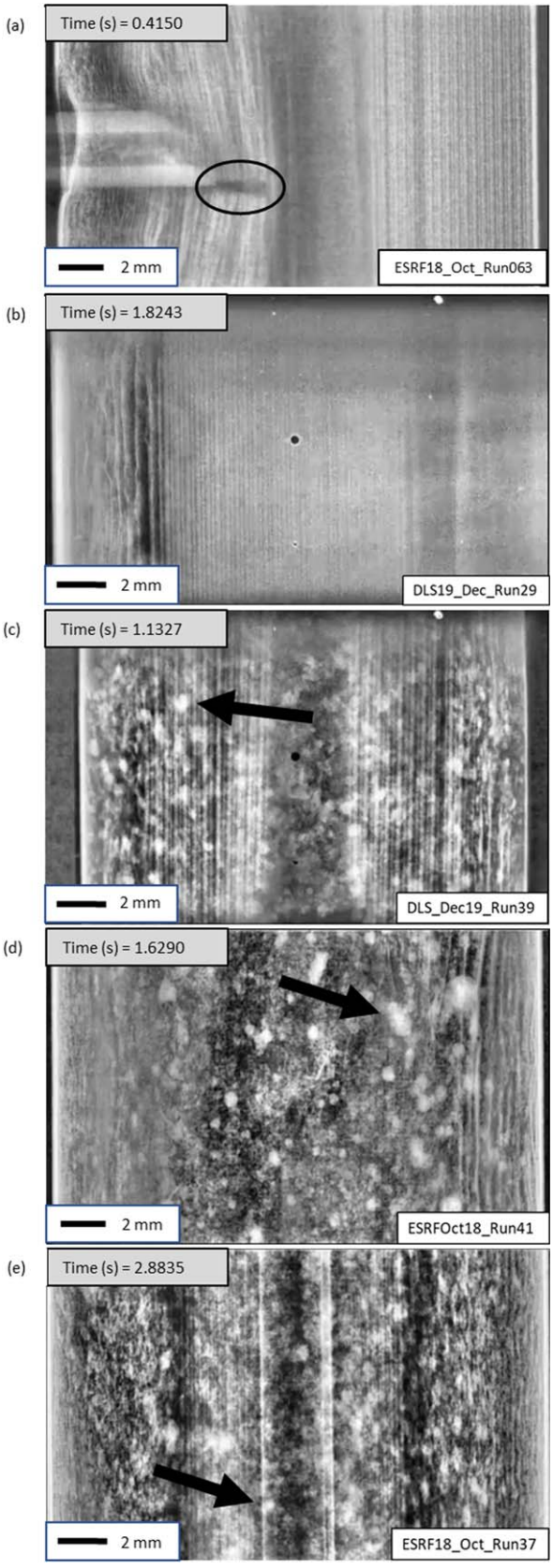

Figure 7. Phenomena of interest elucidated from radiography videos. (a) Innermost layers of the LG 21700 cracking when thermal runaway was initiated by the nail penetration trigger method. Following are radiographs of Saft D-Cell (b), KULR 18650 (c), LG 21700 (d), and KULR 21700 (e) showing evidence of molten copper present in each cell during thermal runaway (black arrows).

example of a cell that clearly displayed molten copper, but whose thermocouple reading did not exceed 300 °C.

The disparity between the thermocouple data and the radiography videos demonstrates a glaring reality regarding the experimental reliability of using nails embedded with thermocouples for internal temperature measurement during thermal runaway. It is clear that this methodology, which is often used to gather data for modelling and simulation, does not provide an accurate measurement of the internal temperature of the cell during thermal runaway. This is likely due to the relatively low thermal conductivity of steel, which means that the temperature of the tip of the nail is unable to reach thermal equilibrium with the cell within the timescale of the experiment. This work therefore demonstrates that temperature measurements conducted in this manner may lead to non-representative data and should be treated with caution. Since the data from the thermocouple within the nail was distinct from the rest of the thermocouples attached around the calorimeter, this erroneous temperature measurement did not influence the error of other heat output measurements.

When comparing to previous literature that used similar nail designs,[17,20,25] it is seen that the peak temperature recorded by the nail reaches its maximum temperature around 5–15 s following initiation of thermal runaway. Here, we see via radiography that Cu melts within around 1 s following initiation of thermal runaway and that thermal runaway lasts for around 2 s. This indicates that the response time of thermocouples embedded in nails in previous work was likely slower than that needed to record the actual peak temperature that most likely occurred around 1–2 s following initiation of thermal runaway. It is seen in Fig. 8a that in general, plots with greater times to peak temperature had lower peak temperature readings. Since all nails here and in previous work were custom made, it is likely that high consistency during manufacturing was not achieved which may affect the response time. For example, differences in the distance of the thermocouple from the tip of the nail of just 100's of micrometers may affect the response time. A thermocouple with a slower response time will record later temperatures where some cooling may have already occurred, thus underestimating the actual peak temperature achieved. Therefore, to assist with future designs of nails embedded with thermocouples, it is advisable for researchers to pay attention to the time to peak temperature following penetration of cells and aim to minimize this time for highest accuracy of peak temperature readings. The green plot in Fig. 8d has a peak time of around 1 s and is therefore considered a reliable result.

Conclusions

To better understand the relationship between cell geometry, thermal runaway trigger method, and mass ejection, thermal runaway was initiated in a variety of Li-ion battery cylindrical cell geometries using different trigger methods while calorimetric, ejected mass, and radiographic data were recorded. With the exception of the D-cell, a positive correlation between the fraction of ejected mass from cells and the total heat output was also observed, where more heat is generated by cells that ejected more mass. When comparing nail penetration tests to thermal abuse tests, it was observed that the normalized heat output (kJ/Ah) was larger for nail peneration than for thermal abuse tests, and the difference increased with increasing cell diameter. Thermal runaway reaction velocity was estimated from radiography videos and showed that while cell geometry had seemingly no impact on the observed velocities, the rate of propagation of thermal runaway did seem to have an impact on the unrecovered mass ejected (smoke) from the cell. Slower reaction-front velocities allowed the reaction to proceed further to completion before the cell contents were ejected. Finally, molten copper (indicating that internal temperatures exceeded 1085 °C, the melting point of copper) was seen in the 18650 and 21700 cells but not in the D-Cell. Temperature measurements made with thermocouples embedded into nails used in nail penetration

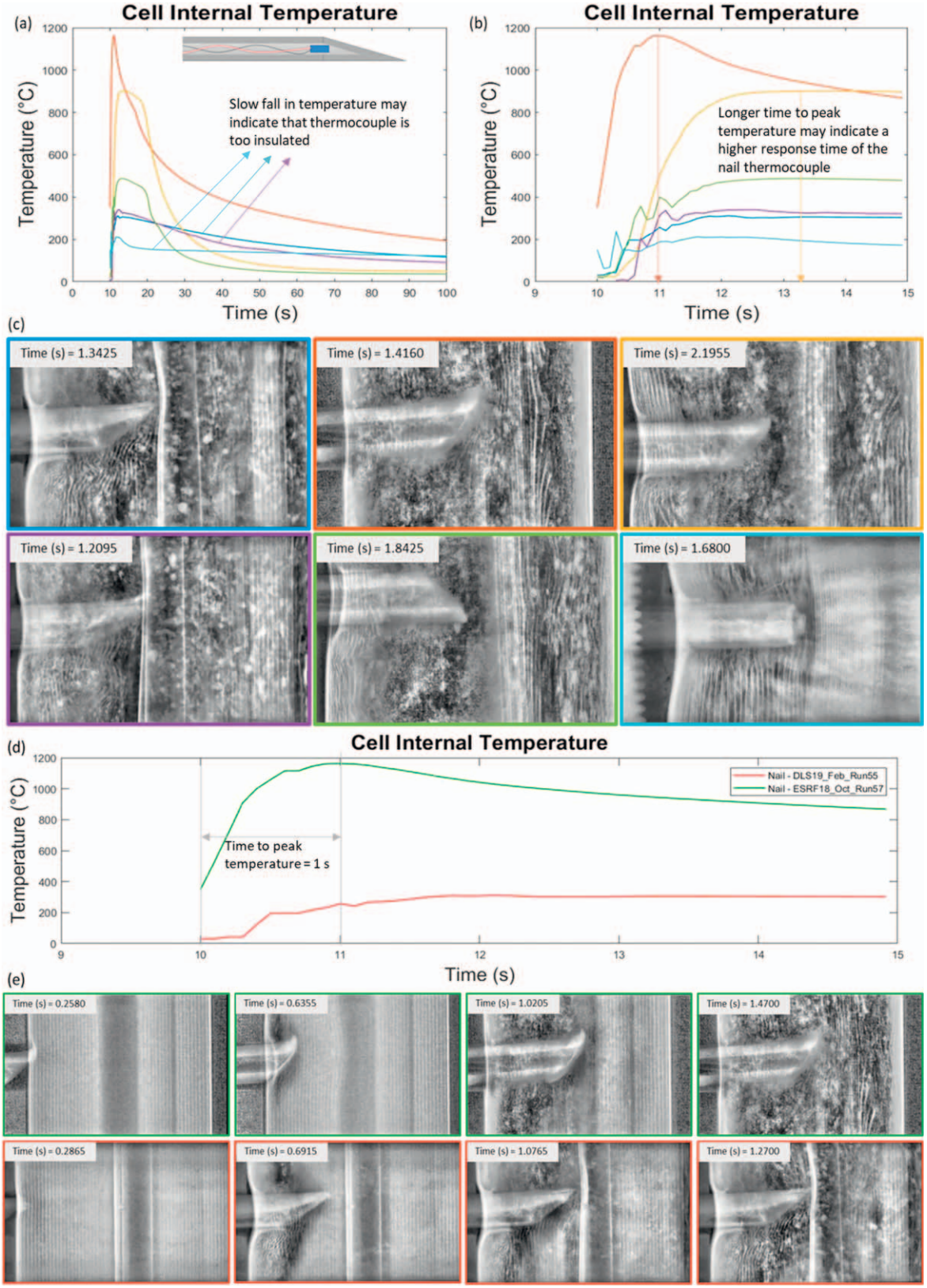

Figure 8. (a) Transient temperature readings obtained using thermocouple embedded nails shown in the inset image. 100 s shown. (b) Magnified view of the first 5 s following thermal runaway initiation. Each test has an associated radiograph shown in (c) where the line color matches with the colored radiograph border. Molten copper can be seen as white globules in all but one radiograph. Time stamps are from around the moment the nail punctured the cell. IDs for the tests shown can be found in Supplementary Information. (d) Temperature readings obtained from thermocouple embedded nails. The green plot shows temperature measurements that reflect the radiography data, whereas the red plot shows an example of the thermocouple embedded nail temperature measurement. Associated radiographs shown in (e) with a green border (first row) and red border (bottom row) respectively where molten copper is clearly visible in the last frame for both tests.

tests were shown to be unreliable, most likely because thermal equilibrium between the tip of the nail and the cell cannot be established on the timescale of the experiment. In summary, the results show that thermal runaway behavior varies for different designs of cells and for different triggering methods (nail penetration, thermal, and ISC). All data is available open source via the Battery Failure Databank.[24]

Acknowledgments

This work was authored by Alliance for Sustainable Energy, LLC, the manager and operator of the National Renewable Energy Laboratory for the U.S. Department of Energy (DOE) under Contract No. DE-AC36-08GO28308. The views expressed in the article do not necessarily represent the views of the DOE or the U.S. Government. The U.S. Government and the publisher, by accepting the article for publication, acknowledges that the U.S. Government retains a nonexclusive, paid-up, irrevocable, worldwide license to publish or reproduce the published form of this work, or allow others to do so, for U.S. Government purposes. These experiments were performed between beamlines ID19 at the ESRF (Grenoble, France) and I12 at Diamond Light Source (Harwell, UK). This work was carried out with the support of Diamond Light Source, instrument I12 (proposals MG24112, EE20903, EE17641). We are grateful to the ESRF and Diamond Light Source for allowing us to use their facilities. This work was also supported in part by the Faraday Institution (EP/S003053/1, Grant FIRG001, FIRG024 and FIRG028) and the National Measurement System of the UK Department of Business, Energy and Industrial Strategy. PRS acknowledges the Royal Academy of Engineering for the Chair in Emerging Technologies (CiET1718/59).

ORCID

Thomas M. M. Heenan https://orcid.org/0000-0001-9912-4772
Rhodri Jervis https://orcid.org/0000-0003-2784-7802
Rhodri Owen https://orcid.org/0000-0002-1246-2988
Du Wenjia https://orcid.org/0000-0001-8434-4764
Alexander Rack https://orcid.org/0000-0001-9486-3621
Eric Darcy https://orcid.org/0000-0002-8426-8607
Paul R. Shearing https://orcid.org/0000-0002-1387-9531
Donal P. Finegan https://orcid.org/0000-0003-4633-560X

References

1. S. Yayathi, W. Walker, D. Doughty, and H. Ardebili, "Energy distributions exhibited during thermal runaway of commercial lithium ion batteries used for human spaceflight applications." *J. Power Sources*, **329**, 197 (2016).
2. J. Deng, C. Bae, J. Marcicki, A. Masias, and T. Miller, "Safety modelling and testing of lithium-ion batteries in electrified vehicles." *Nat. Energy*, **3**, 261 (2018).
3. AAIB, Report on the serious incident to Boeing B787-8, ET-AOP London Heathrow Airport on 12 July 2013. 2015.
4. J. Chamary, "Why are Samsung's Galaxy Note 7 phones exploding?" (2016), (http://forbes.com/sites/jvchamary/2016/09/04/samsung-note7-battery/#27e9d8111eb2).
5. A. Börger, J. Mertens, and H. Wenzl, "Thermal runaway and thermal runaway propagation in batteries: What do we talk about?" *Journal of Energy Storage*, **24**, 100649 (2019).
6. A. W. Golubkov, D. Fuchs, J. Wagner, H. Wiltsche, C. Stangl, G. Fauler, G. Voitic, A. Thaler, and V. Hacker, "Thermal-runaway experiments on consumer Li-ion batteries with metal-oxide and olivin-type cathodes." *RSC Adv.*, **4**, 3633 (2014).
7. D. P. Finegan et al., "Modelling and experiments to identify high-risk failure scenarios for testing the safety of lithium-ion cells." *J. Power Sources*, **417**, 29 (2019).
8. W. Q. Walker, J. J. Darst, D. P. Finegan, G. A. Bayles, K. L. Johnson, E. C. Darcy, and S. L. Rickman, "Decoupling of heat generated from ejected and non-ejected contents of 18650-format lithium-ion cells using statistical methods." *J. Power Sources*, **415**, 207 (2019).
9. V. Ruiz, A. Pfrang, A. Kriston, N. Omar, P. Van den Bossche, and L. Boon-Brett, "A review of international abuse testing standards and regulations for lithium ion batteries in electric and hybrid electric vehicles." *Renew. Sustain. Energy Rev.*, **81**, 1427 (2018).
10. B. Lei, W. Zhao, C. Ziebert, N. Uhlmann, M. Rohde, and H. J. Seifert, "Experimental analysis of thermal runaway in 18650 cylindrical li-ion cells using an accelerating rate calorimeter." *Batteries*, **3**, 2 (2017).
11. S. Zheng, L. Wang, X. Feng, and X. He, "Probing the heat sources during thermal runaway process by thermal analysis of different battery chemistries." *J. Power Sources*, **378**, 527 (2018).
12. J. K. Ostanek, W. Li, P. P. Mukherjee, K. R. Crompton, and C. Hacker, "Simulating onset and evolution of thermal runaway in Li-ion cells using a coupled thermal and venting model." *Appl. Energy*, **268**, 114972 (2020).
13. P. T. Coman, S. Rayman, and R. E. White, "A lumped model of venting during thermal runaway in a cylindrical lithium cobalt oxide lithium-ion cell." *J. Power Sources*, **307**, 56 (2016).
14. J. Lamb, L. Torres-Castro, J. C. Hewson, R. C. Shurtz, and Y. Preger, "Investigating the role of energy density in thermal runaway of lithium-ion batteries with accelerating rate calorimetry." *J. Electrochem. Soc.*, **168**, 060516 (2021).
15. X. Feng et al., "Investigating the thermal runaway mechanisms of lithium-ion batteries based on thermal analysis database." *Appl. Energy*, **246**, 53 (2019).
16. D. P. Finegan et al., "Characterising thermal runaway within lithium-ion cells by inducing and monitoring internal short circuits." *Energy Environ. Sci.*, **10**, 1377 (2017).
17. D. P. Finegan, B. Tjaden, M. M. Heenan, T., R. Jervis, M. D. Michiel, A. Rack, G. Hinds, D. J. L. Brett, and P. R. Shearing, "Tracking internal temperature and structural dynamics during nail penetration of lithium-ion cells." *J. Electrochem. Soc.*, **164**, A3285 (2017).
18. D. P. Finegan et al., "Identifying the cause of rupture of li-ion batteries during thermal runaway." *Adv. Sci.*, 1700369 (2017).
19. D. P.;. Finegan et al., "In-operando high-speed tomography of lithium-ion batteries during thermal runaway." *Nat Communications*, **6924**, 6 (2015).
20. T. D. Hatchard, S. Trussler, and J. R. Dahn, "Building a 'smart nail' for penetration tests on Li-ion cells." *J. Power Sources*, **247**, 821 (2014).
21. Battery Failure Databank, 2020, https://nrel.gov/transportation/battery-failure.html.
22. T. L. Barone, T. H. Dubaniewicz, S. A. Friend, I. A. Zlochower, A. D. Bugarski, and N. S. Rayyan, "Lithium-ion battery explosion aerosols: morphology and elemental composition." *Aerosol Sci. Technol.*, **55**, 1183 (2021).
23. V. Premnath, Y. Wang, N. Wright, I. Khalek, and S. Uribe, "Detailed characterization of particle emissions from battery fires." *Aerosol Sci. Technol.*, 1 (2021).
24. Battery Failure Databank. National Renewable Energy Laboratory, 2021, https://nrel.gov/transportation/battery-failure.html.
25. S. Huang, X. Du, M. Richter, J. Ford, G. M. Cavalheiro, Z. Du, R. T. White, and G. Zhang, "Understanding Li-Ion cell internal short circuit and thermal runaway through small, slow and *In Situ* sensing nail penetration." *J. Electrochem. Soc.*, **167**, 090526 (2020).